The Astrophysical Journal, 891:42 (15pp), 2020 March 1 https://doi.org/10.3847/1538-4357/ab6cf9

Equilibrium Tidal Response of Jupiter: Detectability by the *Juno* Spacecraft

Sean M. Wahl[1], Marzia Parisi[2], William M. Folkner[2], William B. Hubbard[3], and Burkhard Militzer[4]
[1] Department of Earth and Planetary Science, University of California, Berkeley, CA 94720, USA; swahl@berkeley.edu
[2] Jet Propulsion Laboratory, California Institute of Technology, Pasadena, CA 91109, USA; marzia.parisi@jpl.nasa.gov, william.m.folkner@jpl.nasa.gov
[3] Lunar and Planetary Laboratory, The University of Arizona, Tucson, AZ 85721, USA; hubbard@lpl.arizona.edu
[4] Department of Earth and Planetary Science, Department of Astronomy, University of California, Berkeley, CA 94720, USA; militzer@berkeley.edu
Received 2019 October 16; revised 2020 January 7; accepted 2020 January 9; published 2020 March 2

Abstract

An observation of Jupiter's tidal response is anticipated for the ongoing *Juno* spacecraft mission. We combine self-consistent, numerical models of Jupiter's equilibrium tidal response with observed Doppler shifts from the *Juno* gravity science experiment to test the sensitivity of the spacecraft to tides raised by the Galilean satellites and the Sun. The concentric Maclaurin spheroid (CMS) method finds the equilibrium shape and gravity field of a rotating, liquid planet with the tide raised by a satellite, expanded in Love numbers (k_{nm}). We present improvements to the CMS theory that eliminate an unphysical center-of-mass offset and study in detail the convergence behavior of the CMS approach. We demonstrate that the dependence of k_{nm} with orbital distance is important when considering the combined tidal response for Jupiter. Conversely, the details of the interior structure have a negligible influence on k_{nm} for models that match the zonal harmonics J_2, J_4, and J_6, already measured to high precision by *Juno*. As the mission continues, improved coverage of Jupiter's gravity field at different phases of Io's orbit is expected to yield an observed value for the degree-two Love number (k_{22}) and potentially select higher-degree k_{nm}. We present a test of the sensitivity of the *Juno* Doppler signal to the calculated k_{nm}, which suggests the detectability of k_{33}, k_{42}, and k_{31}, in addition to k_{22}. A mismatch of a robust *Juno* observation with the remarkably small range in calculated Io equilibrium, $k_{22} = 0.58976 \pm 0.0001$, would indicate a heretofore uncharacterized dynamic contribution to the tides.

Unified Astronomy Thesaurus concepts: Jupiter (873); Tides (1702); Outer planets (1191); Jovian satellites (872); Planetary interior (1248); Tidal distortion (1697)

Supporting material: machine-readable tables

1. Introduction

Since orbital insertion in 2016 July, the *Juno* spacecraft has yielded robust measurements of even (Folkner et al. 2017) and odd (Iess et al. 2018) zonal harmonics of Jupiter's gravitational field. These high-precision gravity measurements inform our understanding of Jupiter's interior structure (Nettelmann 2017; Wahl et al. 2017b; Debras & Chabrier 2019) and wind structure (Kaspi et al. 2017, 2018; Guillot et al. 2018). As the spacecraft makes additional orbits, it is expected to constrain the tidal response of the planet in terms of the degree-two Love number, k_{22}, and possibly higher-degree k_{nm} as well. Prior knowledge of the higher-degree k_{nm} from theoretical models also aids in the fitting of a gravity solution to the *Juno* Doppler radio measurements.

The concentric Maclaurin spheroid (CMS) method (Hubbard 2012, 2013) is a nonperturbative numerical method for calculating the self-consistent mass distribution and gravity field of a rotating liquid body. In two dimensions, the CMS approach allows efficient and precise exploration of interior structure models (Militzer et al. 2019). In three dimensions, the CMS method permits a precise calculation of equilibrium tidal response, yielding both k_{22} and higher-degree k_{nm} (Wahl et al. 2016, 2017a). The CMS calculations demonstrated a significant effect from the rotational flattening of Jupiter and Saturn, manifesting in an enhanced k_{22} compared with calculations treating the tidal response as a perturbation from a sphere (Gavrilov & Zharkov 1977), as well as splitting of the higher-degree k_{nm}. In this paper, we present improvements to the CMS equilibrium tidal response calculations, including a solution to the unphysical center-of-mass offsets described in Wahl et al. (2017a). We also study in greater detail the convergence behavior of CMS tidal response calculations and how this affects the precision to which we can determine different values of k_{nm} for the four Galilean satellites and the Sun.

A preliminary value of $k_{22} = 0.625 \pm 0.06$ was presented in the *Juno* gravity solution of Iess et al. (2018), consistent with the enhanced value predicted from CMS but not sufficiently precise to fully characterize the nature of the tidal response. In the case of Saturn, astrometric observations (Lainey et al. 2017) yield a k_{22} that is below the value for an equilibrium tide to their reported uncertainty but still enhanced compared to the prediction from perturbation theory applied to a spherical Saturn.

A major outstanding question is whether Jupiter's tidal response can be adequately described by equilibrium theory alone, as addressed in this paper, or whether there is a detectable dynamic contribution to the tides. The equilibrium tidal response treated here assumes that the rotating liquid interior responds instantaneously to the perturbing satellite.[5] In the corotating frame of the planet, we find the equilibrium tidal distortion fully determined by the orbit and k_{nm} calculated for each perturbing satellite. In contrast, dynamic tides are a frequency-dependent response, affected by proximity to resonances, excitation, and waves as the tidal perturbations interact with interior structural features, such as stable layers or

[5] The terms "equilibrium tides" and "static tides" have been used interchangeably to refer to the same phenomenon in the literature. We elect to use "equilibrium" in this paper.

density discontinuities (Marley & Porco 1993; Fuller 2014a, 2014b). Calculations of dynamic tides rely on normal mode calculations (Durante et al. 2017) related to techniques used in asteroseismology (Chaplin & Miglio 2013). While special cases of dynamic tidal response have been shown to result in a small enhancement to k_{22} (Gavrilov & Zharkov 1977), a comprehensive treatment of the dynamic tidal response of a Jovian planet with rotational flattening has not been attempted. However, once an interior model is fitted to the observed zonal harmonic coefficient, J_n, its equilibrium tidal response coefficient, k_{nm}, is determined with little remaining uncertainty. Thus, measurements of k_{nm} that disagree with the equilibrium response are evidence of a dynamic tidal response.

In Wahl et al. (2016), we presented preliminary calculations of Jupiter's equilibrium tidal response for a range of different interior models (Hubbard & Militzer 2016) based on pre-*Juno* knowledge and assumptions about the planet's interior. This included a wide range of models, in part because of a disagreement of the JUP310 gravity solution (Jacobson 2013) with earlier gravity solutions (Campbell & Synnott 1985; Jacobson 2003). The pre-*Juno* gravity solution permitted two- or three-layer interior structure models with a variety of hydrogen–helium equations of state (Saumon & Guillot 2004; Militzer et al. 2008; Nettelmann et al. 2012; Hubbard & Militzer 2016; Miguel et al. 2016). As of the *Juno* gravity solution presented by Iess et al. (2018), there are now precise determinations of the even gravity harmonics up to J_{10} and odd harmonics up to J_9. The low-order, even gravity harmonics J_2, J_4, and J_6 are all determined to $\sim 10^{-8}$ or better. When taken into consideration with state-of-the-art equations of state for hydrogen–helium mixtures (Vorberger et al. 2007; Militzer 2013) and constraints on atmospheric composition and temperature, these low-order harmonics place strong constraints on the viable interior structure models (Nettelmann 2017; Wahl et al. 2017a; Debras & Chabrier 2019; B. Militzer et al. 2020, in preparation), suggesting that Jupiter's interior structure is more complicated the previously thought. Nettelmann (2019) presented calculations of the equilibrium k_{nm} of an interior structural fit to an earlier *Juno* gravity solution (Folkner et al. 2017). In this paper, we present results for the equilibrium tidal response of Jupiter, with the constraints from the most recent *Juno* gravity solution (Iess et al. 2018) and an improved implementation of the CMS method. We consider the ranges in tidal response expected from the uncertainty from the interior structure, deep winds, and measurements of the relevant physical parameters, as well as the numerical precision of the CMS method. Characterizing this uncertainty in modeling the equilibrium tide is necessary to know whether a precise measurement of k_{nm} alone is sufficient to detect a dynamic contribution and distinguish it from the equilibrium contributions.

In Section 2.1 we present an overview of the CMS method focused on the details pertinent to the calculation of the equilibrium tidal response. In Section 2.2 we describe the improvements to the CMS approach for equilibrium tidal calculations and their effect on the calculations. In Section 2.3 we describe the interior models used in this study, as well as our methods for quantifying the possible range of k_{nm} from interior structure and winds. In Section 3.1 we look at the convergence of the CMS models with various parameters to quantify the precision to which different k_{nm} can be predicted. In Section 3.2 we present, in detail, the tidal response of Jupiter to the four Galilean satellites and the Sun and consider *Juno*'s ability to sample that tidal response. Finally, in Section 3.4, we test the sensitivity of the *Juno* Doppler gravity measurements to the calculated k_{nm} and discuss the significance of the higher-degree k_{nm} to the fitting of a gravity solution by the *Juno* gravity science experiment.

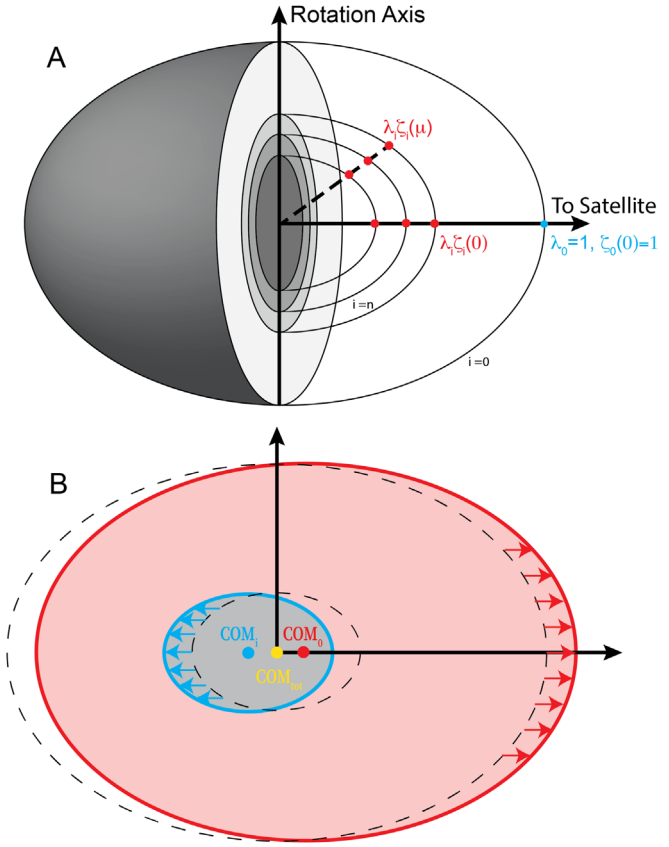

Figure 1. Conceptual diagram of a CMS model with a tidal perturbation from a satellite. (a) The density structure is discretized into a superposition of constant-density spheroids. The surface of spheroid i is described by the fraction ζ_i of the equatorial radius λ_i at coordinates μ, ϕ. (b) In the presence of a tidal perturber, the spheroid surfaces and centers of mass are permitted to respond to the external potential under the constraint of constant volume such that the outermost spheroids shift toward the satellite, while the innermost spheroids shift away from the satellite. The total center of mass remains fixed at the origin.

2. Methods

2.1. CMS Method

The CMS method is a nonperturbative, iterative method for finding the gravity field of a liquid body that was formulated by Hubbard (2012, 2013) and extended to three dimensions by Wahl et al. (2017a).

In this method, a continuous density structure is discretized into N nested, constant-density spheroids, as shown in Figure 1. The planet's self-gravity, V, is calculated as a volume-integrated function of all spheroids in their current configuration and combined with a centrifugal potential, Q, and an external potential from a perturbing satellite, W, into a single effective potential,

$$U(\boldsymbol{r}) = V(\boldsymbol{r}) + Q(\boldsymbol{r}) + W(\boldsymbol{r}). \quad (1)$$

The shape of each spheroid is then adjusted until the surface of each becomes an equipotential surface of U.

Table 1
Jupiter Tidal Parameters

Body	Parameter[a]			Parameter[b]		
Jupiter	GM	126686534.911	$km^3\ s^{-2}$	q_{rot}	$0.089195 \pm 1.5 \times 10^{-5}$	
	r_{eq}	71492 ± 4	km			
	T_{rot}	0:9:55:29.711	D:H:m:s			
Io	GM	5962.0	$km^3\ s^{-2}$	R_{pj}	5.87534	r_J
	a	421769	km	R_{aj}	5.92372	r_J
	e	0.0041		$q_{tid,pj}$	-6.87587×10^{-7}	
				$q_{tid,aj}$	-6.79199×10^{-7}	
Europa	GM	3201.6	$km^3\ s^{-2}$	R_{pj}	9.29196	r_J
	a	671079	km	R_{aj}	9.48158	r_J
	e	0.0101		$q_{tid,pj}$	-9.44995×10^{-8}	
				$q_{tid,aj}$	-9.11439×10^{-8}	
Ganymede	GM	9891.0	$km^3\ s^{-2}$	R_{pj}	14.95833	r_J
	a	1070042.8	km	R_{aj}	14.97629	r_J
	e	0.0006		$q_{tid,pj}$	-6.99812×10^{-8}	
				$q_{tid,aj}$	-6.97297×10^{-8}	
Callisto	GM	7181.3	$km^3\ s^{-2}$	R_{pj}	26.15424	r_J
	a	1883000	km	R_{aj}	26.52298	r_J
	e	0.007		$q_{tid,pj}$	-9.50535×10^{-9}	
				$q_{tid,aj}$	-9.11439×10^{-9}	
Sun	GM	132712440041.93938	$km^3\ s^{-2}$	R_{pj}	10357.8	r_J
	a	778.57×10^6	km	R_{aj}	11422.8	r_J
	e	0.0489		$q_{tid,pj}$	-2.82816×10^{-9}	
			[b]	$q_{tid,aj}$	-2.10853×10^{-9}	

Note.
[a] The physical parameters in the left column are from https://ssd.jpl.nasa.gov/horizons.cgi.
[b] The derived tidal parameters at perijove and apojove.

Given a prescribed interior density structure, the nonspherical contributions to the potential are parameterized by three nondimensional numbers. First is the relative strength of the centrifugal potential,

$$q_{rot} = \frac{\omega^2 r_J^3}{GM_J}, \tag{2}$$

where ω is the sidereal rotation frequency, r_J is the equatorial radius of Jupiter, G is the universal gravitational constant, and M_J is the mass of Jupiter. The second describes the relative strength of the tidal perturbation,

$$q_{tid} = -\frac{3m_s r_J^3}{M_J R^3}, \tag{3}$$

where m_s is the mass of the perturbing satellite (or the Sun) and R is the orbital distance. Last is the ratio of the satellite's orbital distance to the planet's radius,

$$R/r_J. \tag{4}$$

The relevant physical parameters for Jupiter, its satellites, and the Sun are summarized in Table 1. The uncertainty of q_{rot} is dominated by the ~4 km uncertainty in r_J. It is worth noting that although a CMS calculation is performed for a single set of parameters, q_{tid} and R/r_J vary with time due to the eccentricity of the orbit, which must be taken into account when translating the calculated k_{nm} into a gravity signal.

The zonal, J_n, and tesseral, C_{nm} and S_{nm}, harmonics of the gravity field (depicted in Figure 2) can be calculated by integrating over the density and shape of a converged CMS model (Wahl et al. 2017a). For Jupiter and its Galilean satellites, $q_{tid} \ll q_{rot}$, which means that the equilibrium tidal response from each satellite can be calculated independently, and the resulting C_{nm} and S_{nm} can be linearly superimposed to obtain the total equilibrium tidal response. The calculations can be further simplified by assuming that the satellites reside in the planet's equatorial plane, since the Galilean moons each exhibit a small orbital inclination. Under these assumptions, we perform CMS calculations for a single satellite at a time, with a fixed position in the equatorial plane.

As per convention (Zharkov & Trubitsyn 1978), the tidal Love numbers represent the ratio of the tidally induced gravity moments to the strength of the perturbing tidal potential, which can be represented as

$$k_{nm} = -\frac{3}{2}\frac{(n+m)!}{(n-m)!}\frac{(C_{nm} - C^0_{nm})}{P_n^m(0)q_{tid}}\left(\frac{r_{eq}}{R}\right)^{2-n}, \tag{5}$$

where $m \leqslant n$ and P_n^m are the associated Legendre polynomials.[6] Here C^0_{nm} is the harmonic for the unperturbed body (i.e., with rotation but without tides). For $m \neq 0$, $C^0_{nm} = 0$, but

[6] This equation appeared in Wahl et al. (2017a) with a typographical error in the prefactor.

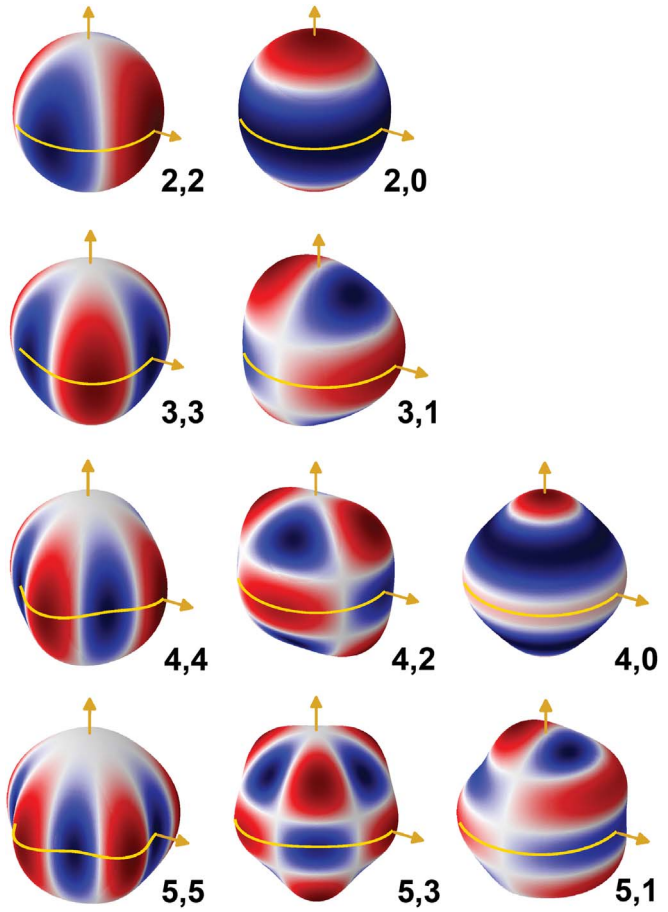

Figure 2. Shapes of the gravity harmonics, C_{nm}, labeled by degree n and order m, where $|m| \leqslant n$. Yellow arrows show the pole and indicate the direction of the tidal perturber, and the yellow line shows the equator.

with rotation

$$C_{n0}^{0} = -2J_{n}^{0}, \tag{6}$$

where J_n is the corresponding zonal harmonics from an axisymmetric calculation with the same $q_{\rm rot}$.

For this reason, the k_{n0} cannot be directly measured in the *Juno* Doppler data, as their contribution is indistinguishable from contributions from rotation and interior density distribution. The eccentricity of the satellite orbit induces a small, time-variable component of C_{n0} that might be detectable as a variation of the observed J_n with the satellite's orbital phase. If the tidal perturbers are located on the equatorial plane, as we assume, then all k_{nm} with odd values of $n - m$ are zero. For a nonrotating planet, the k_{nm} with the same degree n are degenerate with order m. Jupiter, on the other hand, exhibits significant splitting of these k_{nm} due to the significant rotational flattening.

2.2. Tidal Response Calculations

In this section, we provide details to perform accurate tidal response calculation with the CMS method and discuss a number of assumptions and approximations. Most importantly, we only deal with the equilibrium response and assume the planet responds instantaneously to an external perturbation by a satellite. Since the satellite's diameter is small compared to its orbital distance, R, it is well justified to treat the satellite as a point mass, $m_{\rm s}$. Its gravitational potential is given by

$$W(\boldsymbol{r}, \boldsymbol{R}) = \frac{Gm_{\rm s}}{|\boldsymbol{R} - \boldsymbol{r}|} \tag{7}$$

and can be expressed in terms of Legendre polynomials,

$$W(r, \mu, \phi) = \frac{Gm_{\rm s}}{R}\sum_{n=0}^{\infty}\left(\frac{r}{R}\right)^{n}\Bigg[P_n(\mu)P_n(\mu_s) + 2\sum_{m=1}^{n}\frac{(n-m)!}{(n+m)!}\cos(m\phi - m\phi_s)P_n^m(\mu)P_n^m(\mu_s)\Bigg], \tag{8}$$

where we have specified the satellite's location with R, μ_s, and ϕ_s.

For the potential theory to be applicable, the tidal perturbation needs to be time-independent, which means one can only derive the tidal response for an analog system where the satellite's orbital period is set equal to the rotation period of the planet. In the rotating frame, the satellite's gravity field then becomes time-independent, and it is a well-posed but simplified task to determine the planet's response. There are situations where these assumptions are well justified, e.g., tidally locked exoplanets that have equal orbital and rotation periods. However, satellites in the solar system all have orbital periods that are much longer than the rotation periods of the host planets. This introduces a time dependence into the tidal perturbation and may lead to dynamic tidal effects. The dynamic response is typically studied by expanding the planet's response in terms of normal modes (Gavrilov & Zharkov 1977). Even when such dynamic tidal calculations are performed for Jupiter, one expects to find a negligible tidal lag because the viscosity in giant planets is very small. A counterexample is the tides on Earth, where there is a more substantial response lag for the solid mantle and crust.

The standard approach to derive a time-independent solution is to remove the average force that the tidal perturber exerts on the planet (Murray & Dermott 1999). Removing the average force can be motivated by representing the planet by a system of N fluid parcels of mass m_i at locations $\boldsymbol{r}_i$. Its total energy is assumed to be given by $\mathcal{V}(\boldsymbol{r}_1 \ldots \boldsymbol{r}_N)$, and an equilibrium configuration must satisfy $\boldsymbol{F}_i = \partial\mathcal{V}/\partial\boldsymbol{r}_i = 0$. In order to establish the orbital distance for a given planet, we constrain the planet's center of mass to reside at $\boldsymbol{R}_{\rm CM}$. To solve this constrained optimization problem, we introduce the modified function,

$$\tilde{\mathcal{V}}(\boldsymbol{r}_1 \ldots \boldsymbol{r}_N) = \mathcal{V}(\boldsymbol{r}_1 \ldots \boldsymbol{r}_N) - \lambda\left[\sum_i m_i\boldsymbol{r}_i - M\boldsymbol{R}_{\rm CM}\right], \tag{9}$$

where λ is a Lagrange multiplier and M is the total mass. Solving $\partial\tilde{\mathcal{V}}/\partial\boldsymbol{r}_i = 0$ yields that λ must be equal to the average force, $\langle\boldsymbol{F}\rangle$. The equilibrium solution of the constrained system must then satisfy $0 = \partial\mathcal{V}/\partial\boldsymbol{r}_i - \langle\boldsymbol{F}\rangle\, m_i$, which explains why one would want to remove the average force.

In the CMS calculations, we derive this average force as

$$\langle\boldsymbol{F}\rangle = \frac{1}{M}\int d\boldsymbol{r}\ \rho(\boldsymbol{r})\ \nabla_{\boldsymbol{r}}W(\boldsymbol{r}, \boldsymbol{R}) = -\frac{1}{M}\nabla_{\boldsymbol{R}}\int d\boldsymbol{r}\ \rho(\boldsymbol{r})\ W(\boldsymbol{r}, \boldsymbol{R}) = -\frac{m_{\rm s}}{M}\nabla_{\boldsymbol{R}}V(\boldsymbol{r} = \boldsymbol{R}), \tag{10}$$

where we have integrated over all fluid parcels in the planet in the first two terms. In the last term, we have used the symmetry of the gravitational potential, which implies that the average force that the satellite exerts on the planet is equal but opposite to the force that the planet exerts on the satellite. The evaluation of the last term is straightforward within the CMS method because the gradient is already needed to converge the spheroid shapes onto equipotential surfaces using Newton's method.

With the average force, we define a modified tidal potential

$$\tilde{W}(\boldsymbol{r}, \boldsymbol{R}) = W(\boldsymbol{r}, \boldsymbol{R}) - \langle \boldsymbol{F} \rangle \cdot \boldsymbol{r} \tag{11}$$

and introduce it into Equation (1) before using the modified potential to construct equipotential surfaces. With this approach, one obtains a stable numerical algorithm that converges to a self-consistent CMS solution. This algorithm is used for all of the results reported in this paper.

With other, more approximate approaches, it is more difficult to reach well-converged simulations. Zharkov & Trubitsyn (1978) did not derive the average force explicitly but instead removed the $n = 1$ term from Equation (8), which is linear in r. For point masses, this is equivalent to Equation (10), but for an extended planet, this introduces a small spurious force that lets the planet drift toward the satellite because the gravitational force is nonlinear. In the previous implementation of the CMS tidal response calculation (Wahl et al. 2017a) that was based on Equation (8), we noticed a small but persistent center-of-mass shift ($C_{11} > 0$) following each iterative update of the spheroid surfaces (ζ_i). This was accounted for by applying a translation to all grid points after each iteration to eliminate C_{11}, but this prevented full convergence of the spheroids to equipotential surfaces with the expected numerical precision. With our new approach based on Equations (10) and (11), this problem has been eliminated, and we now obtained well-converged equipotentials, and the computed C_{11} is zero to within numerical precision.

We initialize our tidal calculations with spheroid shapes defined by the fractional radius, $\zeta_i(\mu, \phi)$, that we obtain from a fully converged 2D axisymmetric CMS solution, $\zeta_i(\mu)$. The spheroid shapes have converged when $U(\zeta_i(\mu, \phi))$ is the same for all points in any given spheroid. We can no longer fix $\zeta_i(\mu = 0) = 1$, since we expect two tidal bulges to form. Instead, we require the volume of each spheroid to be the same as determined by the initial axisymmetric calculation. Since there is much flexibility in the 3D CMS calculation, the implementation of the volume constraint requires some care. For a given spheroid, we first compute a target potential value, U_i^{T}, by averaging $U(\zeta_i(\mu_k, \phi_k))$ over all spheroid points, k. We then compute the vector of proposed ζ corrections with Newton's method,

$$\Delta\zeta_i^{(k)} \equiv \Delta\zeta_i(\mu_k, \phi_k) = \frac{U(\zeta_i(\mu_k, \phi_k)) - U_i^{\mathrm{T}}}{U'(\zeta_i(\mu_k, \phi_k))}, \tag{12}$$

where U' is the derivative of U with respect to ζ. We require that all $\Delta\zeta_i^{(k)}$ combined do not change the spheroid volume, Ω_i. We thus remove the volume-changing vector component with

$$\boldsymbol{y}^{\mathrm{corr}} = \boldsymbol{y} - \frac{\boldsymbol{y} \cdot \boldsymbol{x}}{\boldsymbol{x} \cdot \boldsymbol{x}} \boldsymbol{x}, \tag{13}$$

where $\boldsymbol{y}$ and $\boldsymbol{x}$ represent the vectors $\Delta\zeta_i^{(k)}$ and $d\Omega_i / d\zeta_i^{(k)}$, respectively. We then apply the corrected $\boldsymbol{y}^{\mathrm{corr}} \equiv \Delta\zeta_i^{(k)}$ and rescale the spheroid again to exactly match the original Ω_i.

Once all spheroids have been updated, we compute the new C_{11} term and apply a single coherent shift to all spheroids so that the planet's total center of mass is again at the origin. This requires performing a spline interpolation for each spheroid over μ and ϕ so that the pre- and postshift grid points remain on the quadrature points. In contrast to the behavior described in Wahl et al. (2017a), this center-of-mass shift gradually decreases to zero as the spheroids converge toward equipotential surfaces.

When we examine the converged CMS solutions, we notice that the centers of mass of individual outer spheroids exhibit a small shift toward the perturbing satellite, while the inner spheroids have drifted away from it, as shown in Figure 1(b). When we instead restricted the center of mass of every individual spheroid during the CMS iterations, we were not able to construct equipotential surfaces. We thus conclude that the small spheroid shifts are necessary to correctly represent how a fluid planet with a realistic interior density structure responds to the tidal perturbations.

In Figure 3, we show the spheroid shifts quantitatively for a representative CMS calculation. Over the course of the calculations, the spheroids arrange themselves so that the centers of mass follow a smooth function of radius. When shown as a function of integrated mass, it can be seen that roughly half of the mass is shifted toward the satellite and the other half away, such that the planet's total center of mass remains at the origin. The inner spheroids exhibit a larger magnitude of shift than the outer spheroids, but they also contain less mass. Depending on the magnitude of the tidal perturbation, we find that the outermost spheroid shifts between 10^{-12} and 10^{-5} Jupiter radii.

2.3. Interior Models

We start from the assumption of a liquid planet in hydrostatic equilibrium,

$$\nabla P = \rho \nabla U, \tag{14}$$

where P is the pressure, ρ is the mass density, and U is the total effective potential. The material properties of the hydrogen–helium mixture, with a mass fraction of heavier elements in solution, determines a barotrope $P(\rho)$ for the planet's interior.

Presently, the most trusted equations of state are constructed from ab initio simulations using density functional molecular dynamics (DFT-MD; Vorberger et al. 2007; Militzer 2013; Becker et al. 2015; Chabrier et al. 2019). Our models use barotropes constructed from a grid of adiabats determined by the Militzer (2013) equation of state for a hydrogen–helium mixture. The DFT-MD simulations were performed, with cells containing $N_{\mathrm{He}} = 18$ helium and $N_{\mathrm{H}} = 220$ hydrogen atoms, using the Perdew–Burke–Ernzerhof functional (Perdew et al. 1996) in combination with a thermodynamic integration technique.

There was initial disagreement between different DFT-MD–based equations of state for hydrogen–helium mixtures, with the REOS (Nettelmann et al. 2008; Becker et al. 2015) equation of state predicting hotter, less dense barotropes (Militzer 2009; Guillot et al. 2018) than those of Militzer (2013) due to their different method for calculating the specific entropy. There is now better agreement between the independently constructed

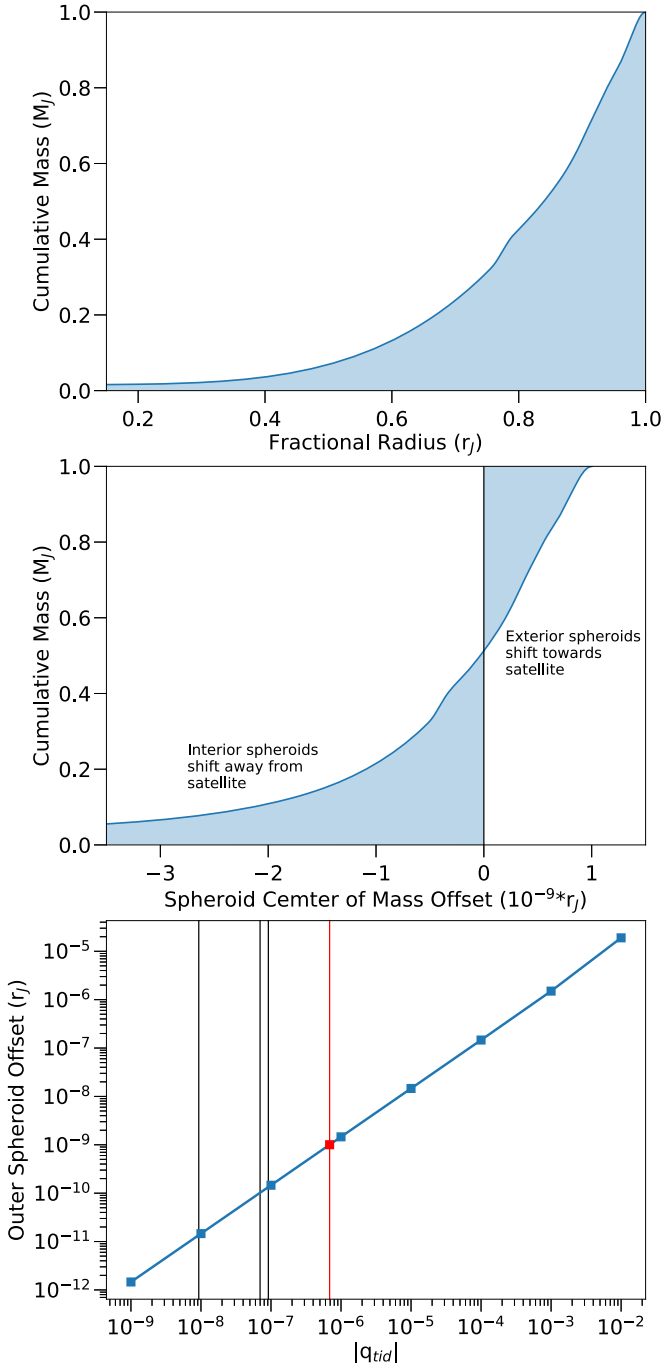

Figure 3. Top panel: cumulative mass m/M_J as a function of fractional radius λ for a representative interior model. Middle panel: offset of spheroid center of mass as a function of cumulative mass for CMS models with tidal response to Io. Spheroids exterior to $m/M_J \sim 0.5$ have center-of-mass shifts toward the satellite, while interior spheroids have center-of-mass shifts away from the satellite. The total center of mass of the planet is constrained to lie at the origin. Bottom panel: magnitude of the center-of-mass shift for the outermost layer ($\lambda = 0$) as a function of tidal perturber strength, $q_{\rm tid}$. Vertical lines denote the $q_{\rm tid}$ of the four Galilean moons, with Io shown in red.

DFT equations of state (Militzer & Hubbard 2013; Schöttler & Redmer 2018; Chabrier et al. 2019), all predicting colder, denser barotropes consistent with those based on thermodynamic integration.

We follow the same treatment of specific entropy, helium, and heavy-element fractions as in previous work (Hubbard & Militzer 2016; Militzer et al. 2016; Wahl et al. 2016, 2017b). The entropy, S, is a proxy for a particular adiabatic temperature T (P) relationship for a fixed composition H–He mixture ($Y_0 = 0.245$). This initial composition also provides the reference barotrope densities, in which deviations from the baseline composition ($Y_0 = 0.245$, $Z_0 = 0$) are treated as perturbations using the additive volume law (Wahl et al. 2017a).

When the inherent density of the hydrogen–helium mixture is set by the DFT equation of state, it is not possible to find simple three-layer interior models that simultaneously match the *Juno* gravity solution while satisfying the atmospheric constraints on temperature and composition from the *Galileo* entry probe (Seiff et al. 1998; von Zahn et al. 1998). Satisfying all such constraints requires either more complex interior thermal and compositional structure (Debras & Chabrier 2019), contributions from deep winds (Guillot et al. 2018; Kaspi et al. 2018), or both (B. Militzer et al. 2020, in preparation). The requisite deep wind profile decays with depth due to interaction of the conductive fluid with the magnetic field (Cao & Stevenson 2017) and cannot be described self-consistently using a potential-based theory like CMS (Militzer et al. 2019).

The Love numbers are known to be strongly correlated with J_n (Wahl et al. 2017a). We thus elect to first examine a set of simple interior models capable of matching the updated low-order axisymmetric *Juno* gravity solution (Iess et al. 2018) with loosened compositional constraints (A1–4 in Table 2). We next consider the effect of deep wind profiles optimized to match the odd zonal harmonics (Kaspi et al. 2018; B1–2 in Table 2). Finally, we include models in which a more complicated interior structure and deep wind profile are optimized simultaneously (B. Militzer et al. 2020, in preparation; C1–4 in Table 2). The models considering deep winds are described in more detail in Section 2.4.

The first set of models considered are three- or four-layer interior models modified from those presented in Wahl et al. (2017b) with parameters tuned to match J_2, J_4, and J_6. These models are denoted as A1–4 in Table 2, with model J_n compared to the target values from *Juno*. The target J_n are obtained from the Iess et al. (2018) gravity solution to the *Juno* Doppler measurements. However, in this solution, the reported J_n would include any tidal contribution (C_{n0}). Thus, for consistency, we subtract the calculated Io C_{n0} from the observed J_n to obtain the target J_n. For instance, the target $J_2 = 14696.51 \times 10^{-6}$ is used instead of the observed $J_2 = 14696.57 \times 10^{-6}$. The interior models consist of an outer molecular envelope and an inner metallic envelope separated by a transition in which helium is proposed to phase separate and rain out (Stevenson & Salpeter 1977; Morales et al. 2013; Militzer et al. 2016). Each model includes an innermost spheroid representing a constant-density central core with a fractional radius $r/r_j = 0.15$. The outer and inner envelope are parameterized by a set of parameters (S_1, Y_1, Z_1) and (S_2, Y_2, Z_2), respectively. The helium rain region is treated as a smooth transition of each parameter between two pressures, while the central core is treated separately from the envelope parameters with its density required to conserve the total mass of the planet. A subset of these models (A3–A4) also consider a dilute core with a constant enrichment of heavy elements (Z_3) with a higher concentration than in the metallic envelope (Z_2). Since there is a density trade-off between parameters and a lack of constraints in the deep interior, we assume $S_3 = S_2$ and $Y_3 = Y_2$ for simplicity.

Table 2
Interior Models

Model[a]	Description	J_2	J_4	J_6	J_8	J_{10}
Target J_n	PJ06 gravity solution[b]	**14696.51**	**−586.60**	**34.20**	−2.42	0.17
A1	Helium rain onset pressure	14696.51	−586.613	34.202	−2.458	0.202
A2	Helium rain layer ΔS	14696.51	−586.609	34.202	−2.458	0.202
A3	Dilute core Z, $r = 0.7$	14696.51	−586.602	34.204	−2.457	0.202
A4	Dilute core Z, $r = 0.5$	14696.51	−586.603	34.203	−2.457	0.202
B1	Kaspi et al. (2018) longitude-independent	14696.01	−586.561	34.200	−2.459	0.202
B2	Kaspi et al. (2018) longitude-dependent	14697.04	−586.463	34.200	−2.460	0.202
C1	B. Militzer et al. (2020, in preparation) model 1	14694.90	−586.524	34.502	−2.504	0.207
C2	B. Militzer et al. (2020, in preparation) model 2	14695.27	−586.721	34.511	−2.505	0.207
C3	B. Militzer et al. (2020, in preparation) model 3	14694.92	−586.562	34.499	−2.504	0.207
C4	B. Militzer et al. (2020, in preparation) model 4	14695.08	−586.566	34.503	−2.504	0.207

Notes.
[a] All A and B models fit J_2 and J_4 by tuning S and $Z2$. Descriptions for A models specify the parameter tuned to fit J_6. The B models are fit to the ΔJ_n from Kaspi et al. (2018) optimized wind profiles. The C models are more complicated interior profiles from B. Militzer et al. (2020, in preparation), where ΔJ_n corresponds to a wind profile optimized simultaneously with the interior density profile. Model A1 is used as the reference model in all tables and figures unless otherwise stated.
[b] Target J_n is from the PJ06 gravity solution (Iess et al. 2018) with the calculated tidal contribution from Io removed. The J_n values which models A1–A4 attempt to match are shown in bold.

In model A1, J_2 and J_4 are matched by iteratively tuning $S_1 = S_2$ and Z_2 and J_6 by tuning the pressure of helium rain onset. In other models, the pressure of helium rain onset is set to $P = 95.4$ GPa, consistent with the Morales et al. (2013) phase curve and an outer envelope adiabat with $S = 7.07\ k_B$ electron^{-1} based on *Galileo* entry probe temperature measurements (Seiff et al. 1998).[7] In model A2, J_2 and J_4 are matched to the same procedure, while J_6 is matched by tuning the jump in $\Delta S = S_2 - S_1$ across the helium rain layer. Finally, models A3 and A4 fit J_6 by tuning the heavy-element fraction of a dilute core, Z_3, with a fractional radius of $r/r_j = 0.7$ and 0.5, respectively. Models A3 and A4 require dilute cores with $Z_3 = 0.12$ and 0.30, respectively, compared to the heavy-element fraction for the deep envelope with $Z_2 = 0.066$ in A1.

As noted previously (Wahl et al. 2017b; Guillot et al. 2018), such simple three- or four-layer models require outer envelopes hotter than expected based on the *Galileo* entry probe measurements (Seiff et al. 1998) when using the Militzer (2013) equation of state. These models are thus interpreted to give a rough, conservative estimate of the range of tidal responses that might be expected from variability in an interior density structure alone matching the low-order zonal harmonics, rather than seeking a single model to match all desired constraints.

2.4. Influence of Deep Winds

The observed zonal harmonics are not due solely to a barotropic interior profile but will have contributions from deep winds (Kaspi 2013; Kaspi et al. 2017). Due to the limitations of potential theory, differential rotation can only be implemented fully consistently for cylinders extending through the deep interior of the planet (Wisdom & Hubbard 2016). It is therefore not possible to implement the more complex 3D wind profile expected for Jupiter, in which the cylindrical flow velocities decay rapidly at depths where conductivity becomes high enough for flows to couple to the planet's magnetic field (Cao & Stevenson 2017). We therefore cannot self-consistently test their effect on the tidal response (Militzer et al. 2019). As a conservative estimate, we consider interior models that fit to $J_2 - J_6$ with the contributions from various wind models omitted. The first class of wind models uses the ΔJ_n from Kaspi et al. (2018), which used the thermal wind equation (TWE) to optimize a decay function for the observed surface wind profiles to match the odd zonal harmonics. The second class of wind models represents a class of models that can be found when the interior structure and wind profiles are optimized simultaneously (B. Militzer et al. 2020, in preparation).

The second set of models in Table 2 are constructed identically to the reference model (A1) but with the target J_n chosen to be $J_{n,Juno} - \Delta J_n$, where ΔJ_n is set to the contribution from the optimized deep wind profiles of Kaspi et al. (2018) for the longitude-independent (model B1) and longitude-dependent (model B2) profiles. The wind profiles that lead to these ΔJ_n values are incompatible with a potential theory–based method like CMS. In lieu of a consistent method for predicting the wind contribution to the tidal response, we consider the case where the winds have no direct contribution to k_{nm} and only affect the model through modifying the target J_n in the CMS calculation to be different from the reference model, A1. Since the true contribution of the winds to k_{nm} should partially offset this difference, this treatment should lead to a conservative estimate of the range values that might result from models with winds. In Section 3.2, we demonstrate that this range is indeed small compared to *Juno*'s sensitivity.

Finally, we calculate the tidal response for a third set of interior models (C1–C4 in Table 2) selected from an ensemble of models generated by a simultaneous optimization of the interior structure and wind profile using a Monte Carlo approach (B. Militzer et al. 2020, in preparation). These models relate wind velocity–depth profiles to contributions in J_n using the TWE as presented in Kaspi et al. (2018). Whereas models B1–B2 from Kaspi et al. (2018) used a single reference interior density structure and found an optimized wind profile to match the odd zonal harmonics (J_3, J_5, ...), models C1–C4

[7] This pressure is not consistent with the envelope entropy for the three or four models presented here, but we treat $P = 95.4$ GPa as a baseline, given multiple sources of uncertainty for the onset of helium rain.

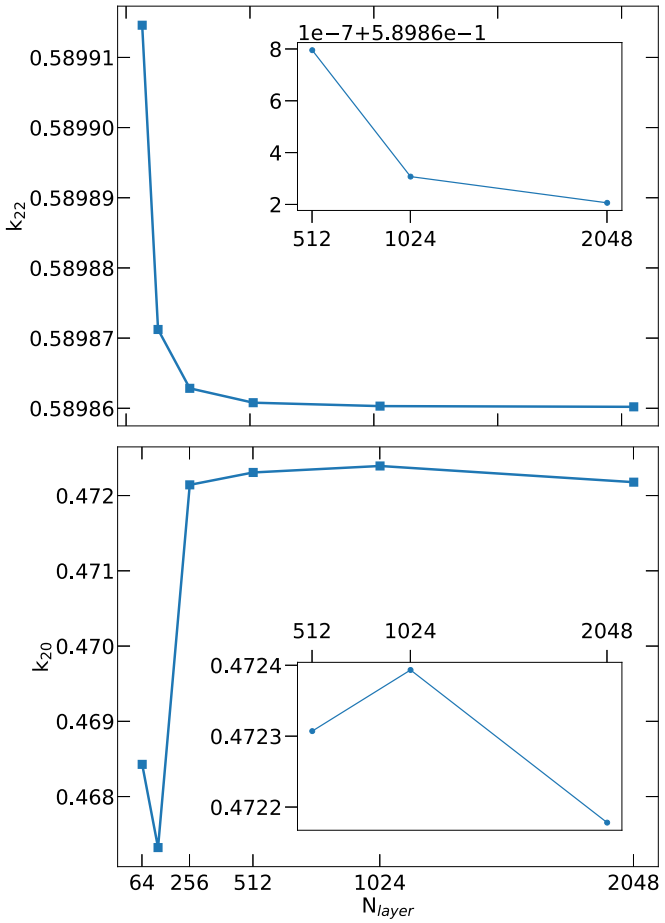

Figure 4. Convergence of Love numbers k_{22} and k_{20} with the number of spheroids, N_L, in the CMS model. The numerical precision for Love numbers of different degree and order is limited by their convergence at $N_L = 512$. The Love numbers of order $m = 0$ are determined to significantly lower precision that the other Love numbers.

attempt to match the even J_n with a combined contribution from the CMS interior structure and a wind profile using the TWE while simultaneously matching the odd J_n with the same wind profile. The parameterization of the interior structure in these models is similar to Wahl et al. (2017b). In practice, these models are found to be able to match the *Juno* J_n while better fulfilling the composition constraints from *Galileo* due to the added freedom for the wind profile to account for a portion of the even J_n. These models result in larger ΔJ_n than Kaspi et al. (2018), particularly for J_6, and consequently lead to a slightly larger range in calculated k_{nm}.

3. Results

3.1. Convergence Behavior

Here we study the convergence behavior of the CMS calculations for the equilibrium tidal response. This is of particular relevance when considering the higher-degree Love numbers, as the tesseral moments of various degree, n, and order, m, can exhibit very different convergence behavior. This must be accounted for when reporting the numerical precision of a given k_{nm} calculated using the CMS approach.

First, we study the discretization error by comparing the calculated k_{nm} for models for an increasing number of spheroids, N_L, in the CMS calculation. Figure 4 shows the convergence of the calculated k_{22} and k_{20} from 64 layers to the 512 layer model used in the rest of the paper, and then up to 2048 layers. The difference between 512 and 1024 layers in the upper panel shows that 512 layers is sufficient to derive k_{22} to six significant digits. Meanwhile, k_{20} is only converged to the level of $\sim 10^{-4}$. The convergence behavior of k_{22} is notably better than that of the higher-degree Love numbers, which converge to $\sim 10^{-5}$ when $n = m$ but with precision worsening as $n - m$ increases. Up to degree $n = 5$, all k_{nm} values are converged with N_L to better than 2×10^{-4}. In the current implementation, calculations of more than 1000 layers are too computationally expensive for a detailed study, although the accelerated approach for the 2D CMS approach (Militzer et al. 2019) could be adapted to the 3D CMS method.

Next, we study the convergence behavior of the various k_{nm} from a single model through the iterative procedure. Whereas the Love numbers with order $m \neq 1$ are converged to at least the level of the discretization error after 25 iterations, those with $m = 1$ require $\sim$150 iterations. This can be attributed to the fact that the rearranging of the spheroid centers of mass described in Section 2.2 is slower than the convergence of the shape of the spheroid. In the original implementation of the CMS tidal response (Wahl et al. 2016, 2017a), the convergence of k_{31} and k_{51} was essentially halted at a precision of $\sim 10^{-2}$ to $\sim 10^{-3}$. This appears to have a negligible effect on the results for the other k_{nm} values, where $n \neq 1$. The convergence behavior over the course of the calculation is also found to be nearly independent of the strength of the tidal perturber $q_{\rm tid}$.

Finally, we look at the convergence behavior of k_{nm} with tidal perturber strength, $q_{\rm tid}$. Figure 5 shows three examples for the convergence of a given k_{nm}, where the satellite's orbital distance is fixed, while $q_{\rm tid}$ or, equivalently, the satellite mass is varied. Starting from a magnitude of $q_{\rm tid}$ much greater than the corresponding satellite value, the value of $k_{\rm nm}$ initially approaches a constant value with decreasing $|q_{\rm tid}|$. This constant demonstrates the expected tidal response in the limit of small perturbation. However, at the smallest values of $|q_{\rm tid}|$, the value of k_{nm} diverges again from the constant value due to the limited numerical precision of the calculation. In the case of Io's k_{22}, the CMS calculation can clearly resolve a small nonlinearity at the corresponding $q_{\rm tid}$.

However, the convergence behavior for other k_{nm} values with $q_{\rm tid}$ differ significantly from k_{22}. From the very same CMS calculation at Io's orbital distance, the value of k_{20} at the satellite $q_{\rm tid}$ is affected by this limited precision. In this case, we cannot resolve any nonlinearity in k_{20}, and we instead report the linear regime value evaluated at the $q_{\rm tid} \sim -10^{-5}$, where the change in k_{20} between different $q_{\rm tid}$ is at a minimum. In Figure 5, the reported k_{nm} is shown in green. The precision of this k_{nm} is limited by the fact that it is derived by taking the finite difference of Equation (5) between two calculations performed with different $q_{\rm tid}$. This uncertainty in the calculated linear regime k_{nm} limits the precision of k_{20} and the other k_{n0} and is included in the reported numerical uncertainty.

The precision of the higher-degree k_{nm} becomes increasingly limited as the satellite becomes more distant due to the decrease in $q_{\rm tid}$. For example, the reported k_{33} for Callisto is the linear regime result, whereas the larger $q_{\rm tid}$ of Io or Europa allows k_{33} to be calculated directly. These limits to the precision of the linear regime k_{nm} calculation are well below the potential sensitivity of *Juno*. The sensitivity of *Juno* is discussed in detail in Sections 3.3

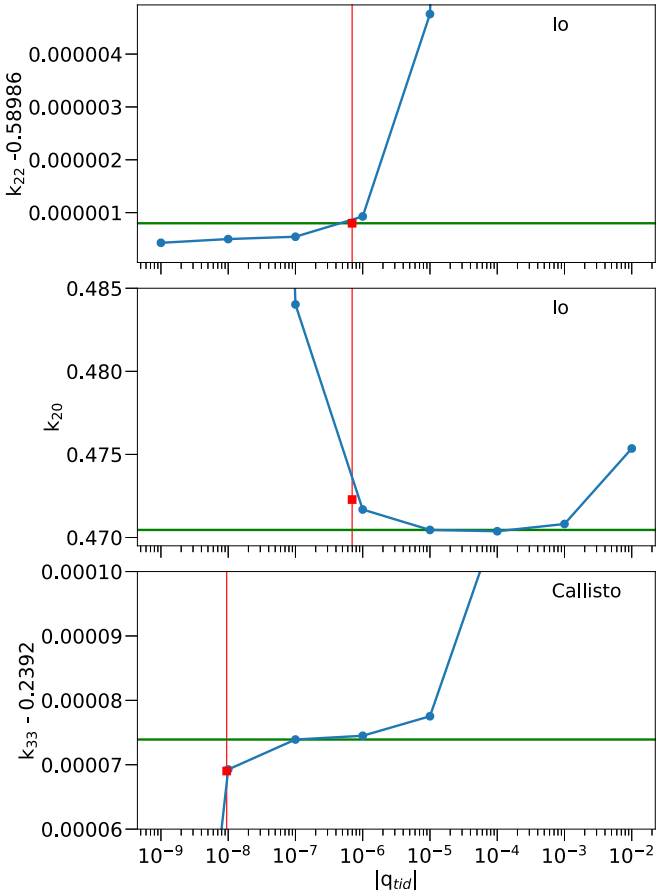

Figure 5. Representative examples of the convergence of various Love numbers as a function of tidal perturber strength, $q_{\rm tid}$ (blue). The red vertical line denotes the value of $q_{\rm tid}$ corresponding to the perturbing satellite. Shown in red is the value obtained directly from the CMS simulation with $|q_{\rm tid}|$ corresponding to the satellite. Shown in green is the reported value for k_{nm}, which depends on whether the CMS simulation at the correct $q_{\rm tid}$ resolves a value better than the estimate for the linear regime. Top: k_{22} for a satellite at Io's orbital distance, which resolves the nonlinearity of the Love number. Middle: k_{20} for a satellite at Io's orbital distance. In this case, the best estimate of the linear regime occurs at $q_{\rm tid,io}$. This is the case for all Love numbers of order zero regardless of satellite. Bottom: For Callisto, the smaller magnitude of $q_{\rm tid}$ means the best estimate of k_{33} is the estimate of the linear regime, even though the k_{33} value is resolved directly for Io.

and 3.4 but can be estimated by taking a relatively optimistic assumption that *Juno* can detect a signal with a maximum strength of ∼1 μgal. If the signal from C_{20} considered in Figure 5 were modified to account for a 1 μgal change in the maximum anomaly, it would cause a corresponding ∼0.01 change in k_{20}, which is 2 orders of magnitude larger than the estimated numerical uncertainty. However, directly using the value calculated at the satellite $q_{\rm tid}$ can result in a significant misreporting of some k_{nm} when the magnitude of $q_{\rm tid}$ is sufficiently small.

3.2. Tidal Response from Galilean Satellites

Table 3 tabulates the calculated Love numbers for the equilibrium tidal response of Jupiter to Io. Independent calculations with the identical reference interior model (A1) were performed at the satellite's perijove and apojove, yielding a linear correction with orbital distance, $dk_{nm}/dR_{\rm sat}$, in units of Jupiter's equatorial radius.

The Love numbers for a nonrotating analog planet are also tabulated. As was noted in previous work with the CMS method, the k_{nm} for a nonrotating planet is independent of m, while for the rapidly rotating Jupiter, these values diverge as a result of rotational flattening. The value of $k_{22} = 0.5897$ for the reference Jupiter model with rotation is significantly higher than the nonrotating case with $k_{22} = k_{20} = 0.5364$.

A similar disparity is seen when the CMS result is compared to the Radau–Darwin approximation, commonly used for tides on bodies with less significant rotational flattening. The normalized moment of inertia (C/Ma^2) can be calculated directly from the CMS interior density structure (Hubbard & Militzer 2016). The calculated moment of inertia, $C/Ma^2 = 0.2639$, would correspond to $k_{22} \sim 0.524$ under this approximation.

As described in Section 3.1, the table notes whether the CMS calculation is able to resolve nonlinear behavior with $q_{\rm tid}$. The numerical uncertainty represents the estimated discretization error for the reported 512 layer CMS calculation. In the cases where the nonlinear behavior cannot be resolved at Io's $q_{\rm tid}$, we report the linear regime result and include the corresponding uncertainty in the reported numerical uncertainty. At the strength of Io's perturbation, all values of k_{nm} with $m \neq 0$ can resolve nonlinearity up to a degree $n = 10$, while nonlinearity is not resolved for any k_{nm} with $m = 0$.

For Io specifically, we also considered the full suite of interior models (A1–C4) tuned to fit the observed low-order zonal harmonics J_2, J_4, and J_6, as described in Section 2.3. These are tabulated as "error interior" and in most cases represent a range less than 1 order of magnitude larger than the numerical precision. Likewise, the range for each Love number from the two sets of interior models constructed with consideration of the deep winds (Section 2.4) are tabulated as "error winds K18" and "error winds M19." Even with their density contributions completely omitted, the range of k_{nm} predicted for wind profiles differs from the reference model (A1) by an amount smaller than could be observed by *Juno*. The error reported in "k_{nm} perijove" includes the maximum deviations from the different interior and wind profiles, along with the estimated numerical error and error propagated from uncertainties in physical constants. For k_{22}, the largest source of uncertainty comes not from interior structure or winds but from propagating the ∼4 km uncertainty on Jupiter's observed radius into $q_{\rm rot}$ and thus to the rotational flattening of the body. In spite of our conservative estimates of the various sources of uncertainty, the combined uncertainty remains well below the expected sensitivity of *Juno*. For instance, an optimistic sensitivity of ∼1 μgal suggests an uncertainty two orders of magnitude larger than the greatest disparity in k_{22} between models with different interior structures or winds. This suggests that k_{nm} is extremely well determined by the low-order gravitational harmonics and thus provides little additional information to constrain the deep interior structure of the planet.

Table 3 also presents the value of k_{nm} for the reference interior model at apojove, along with the corresponding derivative with orbital distance, $dk_{nm}/dR_{\rm sat}$. For $n < 4$, the variation in k_{nm} from orbital distance is small compared to the numerical uncertainty and ranges from different interior models. However, in the case of k_{42}, the deviation of k_{nm} between apojove and perijove is much more substantial. The same is true for other higher-degree k_{nm} values, where $m \neq n$, although in most cases, this effect is likely below detectability. The one possible exception is for k_{20}, where, despite $dk_{nm}/dR_{\rm sat}$ being smaller than the reported uncertainties, independent

Table 3
Calculated Equilibrium Love Numbers for Io

n	m	k_{nm} Nonrotating	k_{nm} Perijove[a]	k_{nm} Apojove	$dk_{nm}/dR_{\rm sat}$	Nonlinear	Error Numerical	Error $q_{\rm rot}$	Error Interior	Error Winds K18	Error Winds M20
2	2	0.536369	$0.589759^{+1.1e-04}_{-1.3e-04}$	0.589749	−1.931e−04	True	±4.9e−07	±9.2e−05	$^{+0.0e+00}_{-5.7e-06}$	$^{+2.1e-05}_{-2.5e-05}$	$^{+0.0e+00}_{-3.0e-05}$
2	0		$0.4699^{+7.1e-04}_{-7.8e-04}$	0.4699	−2.745e−04	False	±1.9e−04	±8.4e−05	$^{+1.3e-04}_{-4.9e-04}$	$^{+2.6e-05}_{-1.5e-05}$	$^{+3.1e-04}_{-0.0e+00}$
3	3	0.22434	$0.23948^{+6.8e-05}_{-6.3e-04}$	0.23948	−9.256e−05	True	±1.5e−05	±5.3e−05	$^{+0.0e+00}_{-1.9e-05}$	$^{+0.0e+00}_{-8.8e-05}$	$^{+0.0e+00}_{-5.5e-04}$
3	1		$0.19014^{+5.7e-05}_{-5.7e-04}$	0.19013	−1.556e−04	True	±1.1e−05	±4.5e−05	$^{+0.0e+00}_{-1.4e-05}$	$^{+0.0e+00}_{-7.0e-05}$	$^{+0.0e+00}_{-5.0e-04}$
4	4	0.12786	$0.1353^{+8.8e-04}_{-8.9e-05}$	0.13529	−5.881e−05	True	±1.3e−05	±3.9e−05	$^{+5.8e-05}_{-0.0e+00}$	$^{+0.0e+00}_{-3.7e-05}$	$^{+7.7e-04}_{-0.0e+00}$
4	2		$1.7432^{+1.7e-03}_{-8.5e-04}$	1.7702	5.589e−01	True	±1.1e−04	±2.9e−04	$^{+6.2e-08}_{-6.8e-06}$	$^{+0.0e+00}_{-4.4e-04}$	$^{+1.3e-03}_{-0.0e+00}$
4	0		$1.8231^{+2.3e-03}_{-2.8e-03}$	1.8516	5.886e−01	False	±6.6e−04	±3.4e−04	$^{+4.1e-04}_{-1.4e-03}$	$^{+0.0e+00}_{-4.5e-04}$	$^{+8.8e-04}_{-0.0e+00}$
5	5	0.08354	$0.08806^{+1.2e-03}_{-5.6e-05}$	0.08805	−4.136e−05	True	±1.1e−05	±3.1e−05	$^{+9.1e-06}_{-8.1e-07}$	$^{+0.0e+00}_{-1.3e-05}$	$^{+1.2e-03}_{-0.0e+00}$
5	3		$0.81536^{+6.7e-03}_{-4.6e-04}$	0.82769	2.548e−01	True	±9.1e−05	±1.9e−04	$^{+1.1e-04}_{-0.0e+00}$	$^{+0.0e+00}_{-1.7e-04}$	$^{+6.3e-03}_{-0.0e+00}$
5	1		$0.9406^{+7.3e-03}_{-5.4e-04}$	0.9551	2.998e−01	True	±1.0e−04	±2.4e−04	$^{+1.9e-04}_{-0.0e+00}$	$^{+0.0e+00}_{-2.1e-04}$	$^{+6.7e-03}_{-0.0e+00}$
6	6	0.059081	$0.062151^{+1.2e-03}_{-1.0e-04}$	0.062149	−3.100e−05	True	±9.3e−06	±2.6e−05	$^{+0.0e+00}_{-5.8e-05}$	$^{+1.3e-05}_{-1.1e-05}$	$^{+1.2e-03}_{-0.0e+00}$
6	4		$0.49903^{+8.0e-03}_{-5.2e-04}$	0.50647	1.538e−01	True	±7.0e−05	±1.5e−04	$^{+0.0e+00}_{-2.1e-04}$	$^{+2.4e-05}_{-8.7e-05}$	$^{+7.8e-03}_{-0.0e+00}$
6	2		$5.8999^{+6.1e-02}_{-3.5e-03}$	6.0858	3.842e+00	True	±7.0e−04	±1.0e−03	$^{+0.0e+00}_{-7.8e-04}$	$^{+0.0e+00}_{-9.6e-04}$	$^{+5.9e-02}_{-0.0e+00}$
6	0		$6.826^{+1.1e-01}_{-1.3e-02}$	7.043	4.498e+00	False	±5.6e−03	±1.6e−03	$^{+7.3e-04}_{-4.7e-03}$	$^{+0.0e+00}_{-1.1e-03}$	$^{+1.0e-01}_{-0.0e+00}$

Notes.
[a] The total error of "k_{nm} Perijove" includes uncertainties from the last five columns.
(This table is available in its entirety in machine-readable form.)

calculations yield a signal with consistent amplitude in which the observable J_2 varies by a magnitude similar to *Juno*'s uncertainty (Iess et al. 2018).

For the reference interior model (A1), identical calculations were performed for the three other Galilean satellites (tabulated in Tables 4–6) and the Sun (Table 7). These tables have been truncated to discount k_{nm} values that would produce signals well below the detectability of *Juno*; the full tables (up to $n = 16$) can be found in the supporting data. For these bodies, the reported uncertainty is the numerical uncertainty plus the uncertainty on $q_{\rm rot}$, as reported for Io, but without the additional ranges from different interior density profiles or winds.

The qualitative behavior of k_{nm} is similar between satellites, although the precise values differ due to nonlinearity in the response to both $q_{\rm tid}$ and $R/r_{\rm J}$. As described in Wahl et al. (2016), the rotational flattening of Jupiter leads to a splitting of the k_{nm} values from those calculated for nonrotating analog planets. Most of the low-degree k_{nm} values agree with those presented in Nettelmann (2019). Our calculated value for Io's k_{22} matches theirs to within our reported uncertainty. The largest disparities occur for k_{nm} with $m = 1$, with their values for Io's k_{31} and k_{51} differing from those presented here by ∼30% and ∼15%, respectively. This disparity can likely be attributed to the treatment of the average force and spheroid centers of mass described in Section 2.2, as they used the older CMS implementation that suffered from the offset center of mass. The match between the independent calculations also becomes poorer for k_{nm} with higher-degree n and for more distant satellites, which may reflect the limitations of numerical precision with small $|q_{\rm tid}|$ summarized in Section 3.1. Nonetheless, the good agreement supports our conclusion on the insensitivity of the equilibrium tidal response to the details of the interior model, including those based on a different equation of state.

The magnitude of the splitting becomes more significant with increasing degree n and orbital distance. It is also noteworthy that a higher-degree k_{nm} with $m \neq n$ shows a much greater difference from the nonrotating analog than k_{nm} with $m = n$. This can be related to the geometry of the tesseral harmonics in Figure 2, as harmonics with $m \neq n$ are those that exhibit nodes in longitude and therefore map differently onto a flattened spheroid than those without such nodes.

Figure 6 shows an example of how two such k_{nm} values vary with orbital distance. For k_{22}, the change is relatively modest, with the value predicted for Europa differing by only $\sim 3 \times 10^{-4}$, likely too small a difference to be observable to *Juno* but still an order of magnitude larger than the uncertainty introduced from considering different interior models that fit the observed $J2 - J6$. In contrast, k_{42} at Callisto's orbital distance is over 18 times larger than that for Io. As a result, the satellite-dependent equilibrium tidal response is most readily observable for k_{42}, even though the magnitude of the signal corresponding to k_{22} and k_{33} is larger. In the case of the tide raised by the Sun (Table 7), the splitting of the calculated higher-degree k_{nm} becomes quite extreme, but the corresponding harmonic C_{nm} strength decays rapidly with degree n, such that all C_{nm} values with $n > 2$ are far below the levels detectable by *Juno*. The lack of a substantial satellite dependence for k_{22} does not rule out the possibility of a satellite-dependent dynamic contribution (Notaro et al. 2019). In fact, given the small difference in equilibrium k_{22} calculated for the various satellites, measurement of disparate k_{22} at the different satellite orbital frequencies might be taken as evidence for a dynamic tidal contribution.

In order to model the complete equilibrium tidal bulge on Jupiter, the contributions from all four of the satellites must be taken into account. Since, for each satellite, $q_{\rm tid} \ll q_{\rm rot}$, it is a reasonable assumption to treat the full tesseral harmonic as a linear superposition of contributions from the separate satellites. Rearranging Equations (3) and (5), the contribution

Table 4
Calculated Equilibrium Love Numbers for Europa

n	m	k_{nm} Nonrotating	k_{nm} Perijove	k_{nm} Apojove	$dk_{nm}/dR_{\rm sat}$	Nonlinear	Error Numerical	Error $q_{\rm rot}$
2	2	0.536369	0.589414 ± 9.2e−05	0.589408	−4.782e−05	True	4.7e−07	9.1e−05
2	0		0.469 ± 1.3e−03	0.469	−6.799e−05	False	1.2e−03	8.4e−05
3	3	0.22434	0.23932 ± 6.9e−05	0.23931	−2.288e−05	True	1.5e−05	5.3e−05
3	1		0.18986 ± 5.7e−05	0.18985	−3.849e−05	True	1.1e−05	4.5e−05
4	4	0.12786	0.13519 ± 5.3e−05	0.13520	−1.450e−05	True	1.3e−05	3.9e−05
4	2		4.1975 ± 9.3e−04	4.3662	8.893e−01	True	2.6e−04	6.7e−04
4	0		4.407 ± 9.1e−03	4.584	9.367e−01	False	8.3e−03	8.0e−04
5	5	0.083531	0.087982 ± 3.9e−05	0.087998	−8.086e−06	True	8.3e−06	3.1e−05
5	3		1.9343 ± 6.7e−04	2.0114	4.056e−01	True	2.3e−04	4.4e−04
5	1		2.2570 ± 8.0e−04	2.3477	4.771e−01	True	2.5e−04	5.5e−04

(This table is available in its entirety in machine-readable form.)

Table 5
Calculated Equilibrium Love Numbers for Ganymede

n	m	k_{nm} Nonrotating	k_{nm} Perijove	k_{nm} Apojove	$dk_{nm}/dR_{\rm sat}$	Nonlinear	Error Numerical	Error $q_{\rm rot}$
2	2	0.536369	0.589274 ± 9.2e−05	0.589276	−1.177e−05	True	4.5e−07	9.1e−05
2	0		0.4692 ± 1.0e−03	0.4692	−1.675e−05	False	9.6e−04	8.4e−05
3	3	0.22434	0.23925 ± 6.9e−05	0.23925	−5.506e−06	False	1.6e−05	5.3e−05
3	1		0.18975 ± 5.8e−05	0.18975	−9.348e−06	False	1.3e−05	4.5e−05
4	4	0.12786	0.13515 ± 5.3e−05	0.13516	−2.322e−06	True	1.3e−05	3.9e−05
4	2		10.7058 ± 2.3e−03	10.7315	1.418e+00	True	6.7e−04	1.7e−03
4	0		11.26 ± 1.7e−02	11.29	1.494e+00	False	1.5e−02	2.0e−03
5	5	0.083498	0.087961 ± 3.3e−05	0.087978	−4.765e−05	True	2.1e−06	3.1e−05
5	3		4.9016 ± 1.9e−03	4.9138	6.467e−01	False	7.5e−04	1.1e−03
5	1		5.7480 ± 2.1e−03	5.7622	7.608e−01	False	7.4e−04	1.4e−03

(This table is available in its entirety in machine-readable form.)

Table 6
Calculated Equilibrium Love Numbers for Callisto

n	m	k_{nm} Nonrotating	k_{nm} Perijove	k_{nm} Apojove	$dk_{nm}/dR_{\rm sat}$	Nonlinear	Error Numerical	Error $q_{\rm rot}$
2	2	0.536369	0.589214 ± 9.8e−05	0.589218	−2.165e−06	False	5.0e−07	9.8e−05
2	0		0.469 ± 9.6e−03	0.47	−3.073e−06	False	9.5e−03	1.0e−04
3	3	0.22434	0.23922 ± 4.8e−05	0.23925	−1.060e−06	False	2.8e−05	2.0e−05
3	1		0.18970 ± 4.1e−05	0.18972	−1.702e−06	False	2.1e−05	2.0e−05
4	4	0.12776	0.13513 ± 1.6e−05	0.13518	−1.662e−06	True	1.1e−05	4.7e−06
4	2		32.507 ± 2.2e−03	33.434	2.496e+00	True	2.0e−03	1.6e−04
4	0		34.2 ± 4.9e−01	35.2	2.628e+00	False	4.9e−01	1.6e−03

(This table is available in its entirety in machine-readable form.)

Table 7
Calculated Equilibrium Love Numbers for Solar Tide

n	m	k_{nm} Nonrotating	k_{nm} Perijove	k_{nm} Apojove	$dk_{nm}/dR_{\rm sat}$	Nonlinear	Error Numerical	Error $q_{\rm rot}$
2	2	0.536369	0.589186 ± 9.1e−05	0.589188	1.878e−12	False	4.6e−08	9.1e−05
2	0		0.469 ± 1.3e−03	0.469	−3.756e−12	False	1.2e−03	8.4e−05

(This table is available in its entirety in machine-readable form.)

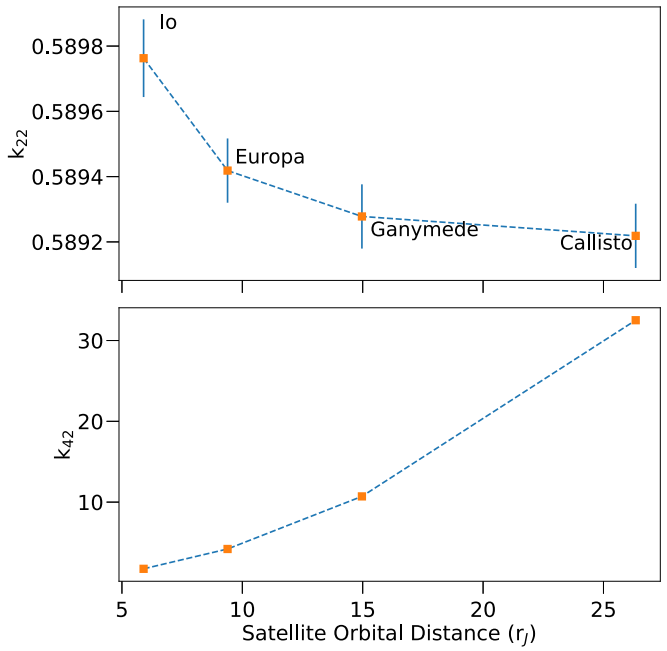

Figure 6. Dependence of Love numbers k_{22} and k_{20} on the orbital distance of the four Galilean moons. The relative strength of the effect becomes more significant for both larger degree n and larger $n - m$. The effect is relatively small for k_{22} (top panel) and more significant for k_{42} (bottom panel). For Io, the error bars show the range of k_{nm} for interior models matching the observed J_n.

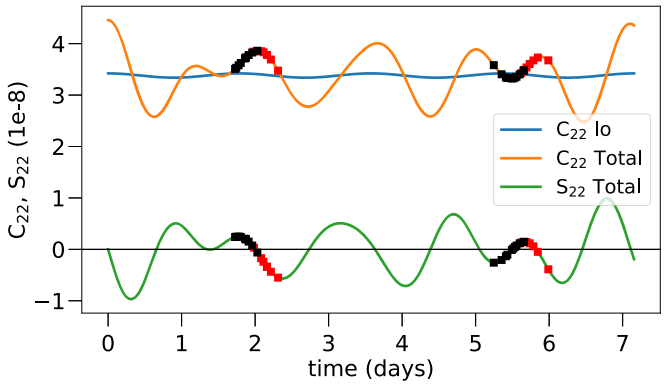

Figure 7. Combined contribution to the tesseral gravity harmonics C_{22} (yellow) and S_{22} (green) from all Galilean moons over the course of one orbit of Ganymede (four orbits of Io), with $t = 0$ at the inferior conjunction of Io and Ganymede. The coordinates are chosen such that Io contributes only to C_{nm}, with S_{nm} contributions arising from the other satellites. The contribution from C_{nm} from Io alone is shown in blue. The squares show the point in the cycle at *Juno* perijove, with completed PJ1–PJ21 in black and projected PJ22–PJ35 in red.

of a satellite to the tesseral harmonics is given by

$$C_{nm} = C_{nm,0} \cos(m(\Phi - \Phi_0), \tag{15}$$

$$S_{nm} = C_{nm,0} \sin(m(\Phi - \Phi_0), \tag{16}$$

where Φ and Φ_0 are the phase of the satellite and a reference phase, and

$$C_{nm,0} = 2\frac{(n-m)!}{(n+m)!}\left(\frac{m_s}{M}\right)\left(\frac{r_{eq}}{R}\right)^{n+1} P_n^m(0) k_{nm}, \tag{17}$$

with k_{nm} at a given orbital separation R given by the various tables. Here R varies over the course of an elliptical orbit, leading to small changes in both r_{eq}/R and q_{tid}.

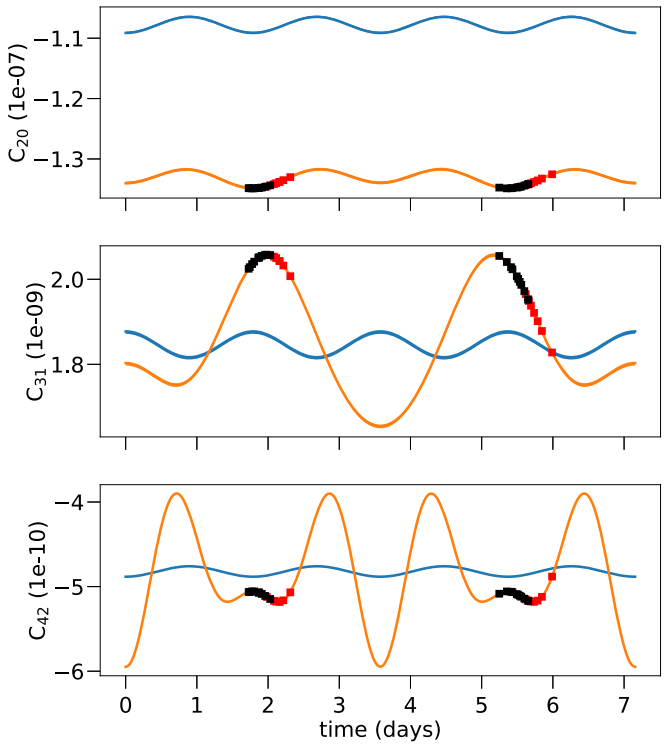

Figure 8. Combined contribution to C_{nm} (yellow) from all Galilean moons over the course of one orbit of Ganymede, as in Figure 7. The contribution from C_{nm} from Io is shown in blue. The squares show the point in the cycle at *Juno* perijove, with completed PJ1–PJ21 in black and projected PJ22–PJ35 in red.

Since the three satellites with the strongest tidal perturbations are in a 4:2:1 orbit resonance, the time-dependent equilibrium tidal bulge is dominated by a signal that repeats once every orbit of Ganymede. It is convenient for visualization to set the reference phase Φ_0 in Equation (15) to that of Io's orbit. In this frame of reference, the primary contribution to the tidal bulge from Io remains fixed, contributing only to C_{nm}, while contributions from the other satellites cause temporal variations in C_{nm} and S_{nm} from that baseline value. Figure 7 shows this repeating pattern in the tidal response in terms of C_{22} and S_{22} over a single orbit of Ganymede, with $t = 0$ taken to be at the inferior conjunction of Io and Ganymede. Figure 8 shows the corresponding pattern for C_{nm} of other selected low-degree harmonics.

Due to the coincidental match of *Juno*'s orbital period with this resonance, the spacecraft perijoves occur within a limited range of $\Phi_{Io} - \Phi_{Europa}$. The point in the orbital cycle for each *Juno* perijove is shown on the C_{nm} curves in Figures 7 and 8 for both the completed (PJ1–PJ21) and currently projected (PJ22–PJ35) perijoves. If the *Juno* spacecraft orbit is altered during the extended mission to allow for a larger range of $\Delta\Phi$, then the sensitivity of the *Juno* gravity solution to the satellite specific k_{nm} would increase.

While k_{20} is not directly observable through the means that k_{nm} with $m > 0$ is, the top panel of Figure 8 suggests an indirect means of measuring it. The equilibrium C_{20} varies with Io's orbital distance. The total equilibrium tidal contribution to J_2 is $\sim 6.6 \times 10^{-8}$ and would be embedded in much larger contributions from the interior or winds. However, the variations from Io's orbital eccentricity would cause the total J_2 to vary by $\sim 1.5 \times 10^{-9}$. This is roughly an order of magnitude smaller than the reported J_2 uncertainty of the

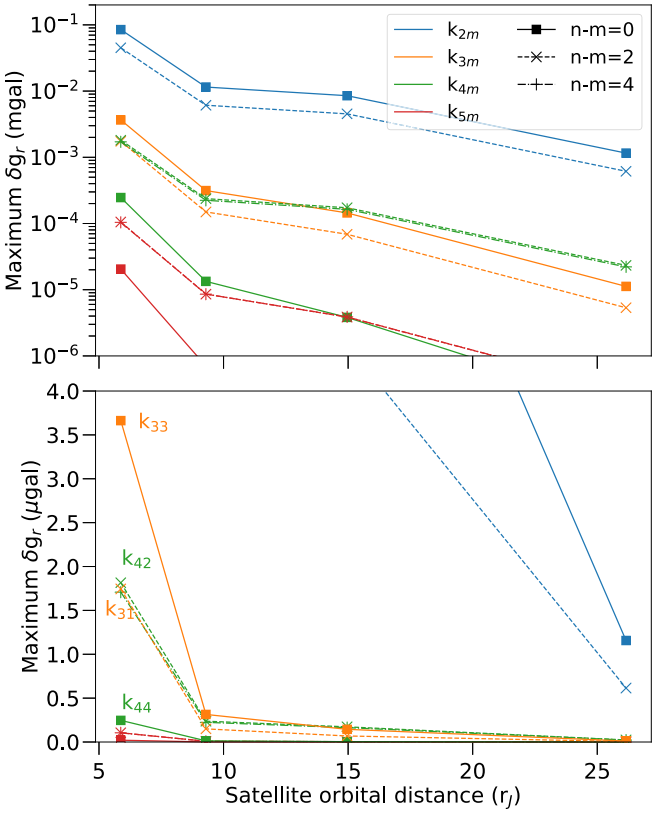

Figure 9. Top panel: maximum gravity anomaly, δg_r, at the surface resulting from the calculated k_{nm} for each Galilean satellite. Bottom panel: same as top panel but on a linear scale at the μgal level. The most readily observable k_{nm} values with $n > 2$ are labeled.

Iess et al. (2018) gravity solution but may become detectable as the uncertainty decreases over the course of the mission.

3.3. Gravity Anomaly from the Love Numbers

A straightforward way of estimating the relative detectability of a given k_{nm} is to calculate the maximum gravitational anomaly associated with that specific Love number. Starting with the corresponding tesseral gravity harmonic C_{nm} from Equation (17), the gravity anomaly at the subsatellite point ($\mu = 0$, $\phi = 0$) that results from adding that tesseral signal to an axisymmetric gravity solution is

$$\delta g_r = C_{nm} \frac{P_n^m(0)}{n+1} \frac{GM_J}{r_J^2}. \tag{18}$$

Figure 9 shows the relative magnitude of the anomaly for various k_{nm} values calculated for each of the four satellites at their perijove. Io's k_{22} yields $\delta g_r \sim 0.085$ mgal, while Europa and Ganymede's k_{22} have a corresponding δg_r roughly 1 order of magnitude smaller, and Callisto's is an order of magnitude smaller yet. In the lower panel of Figure 9, we see that the most readily detectable higher-order Love numbers, k_{33}, k_{42}, and k_{31}, have δg_r values on the order of 1 μgal.

We can attempt to predict which Love numbers *Juno* is sensitive to by comparing the calculated gravity anomaly magnitude with an estimate for observational uncertainty. For instance, Figure 3 of Iess et al. (2018) presents the residual gravitational accelerations for a single close approach of the spacecraft, during which the minimum uncertainty is on the order of ~0.1 mgal. Using this value in conjunction with Figure 9, we would thus predict that *Juno* is sensitive to only k_{22} and k_{20} for Io, and not to any k_{nm} from the other satellites. In the following section, we instead consider the sensitivity to a time-integrated signal from the calculated equilibrium tides.

3.4. Sensitivity of Juno Doppler Measurements to the Calculated Love Numbers

The *Juno* gravity science experiment uses measurements of the Doppler shift of the radio signal transmitted by the spacecraft to determine the time history of the spacecraft velocity projected onto the direction to the Earth tracking station, $\dot{\rho}$. The velocity component is measured with an accuracy of about $\sigma_{\dot{\rho}} = 5\ \mu\mathrm{m\ s^{-1}}$ for averaging times of 1 minute, limited primarily by fluctuations in the water content in the Earth's troposphere (Asmar et al. 2017). The velocity measurements are used to estimate corrections to models of the forces acting on the spacecraft, including Jupiter's equilibrium gravity field and its tidal perturbations characterized by the Love numbers. In order to estimate Love numbers k_{nm} from the Doppler measurements, we calculate the partial derivative for the change in velocity per unit change in the value of the Love number, $\partial\dot{\rho}/\partial k_{nm}$, for each measurement time. Given a calculated value of k_{nm}, the magnitude of the predicted velocity change due to each Love number is

$$\dot{\rho}_{\mathrm{pred}} = k_{nm} \frac{\partial \dot{\rho}}{\partial k_{nm}}. \tag{19}$$

The top panel of Figure 10 shows the predicted Doppler velocity, $\dot{\rho}_{\mathrm{pred}}$, as a function of time for the 13th closest approach of the *Juno* spacecraft to Jupiter (labeled PJ13), on 2018 May 24, due to the tides raised on Jupiter by the four Galilean satellites, each characterized by the calculated values of the Love number k_{42}. The signals are well above the measurement noise level, $\sigma_{\dot{\rho}}$, for about 1 hr centered on closest approach, and, as expected, Io raises the strongest tidal effect on Jupiter. Equivalent signatures from k_{22} are nearly 200 times larger than those from k_{42}; therefore, we choose not to display both effects, as they are difficult to display using the same scale for the signal strength. Eventually, the values of the Love numbers will be adjusted to best fit the measurements from several *Juno* perijoves. While the data are still being calibrated, we use the theoretical values of the Love numbers while estimating the larger equilibrium gravitational signature to reduce the chance of mismodeling of the tidal signatures corrupting the equilibrium gravity field estimate.

The middle panel of Figure 10 shows the degree-four tidal signal from Io during PJ13 for different values of the order m. Likewise, the signals of these parameters are well above the noise cutoff level; hence, we expect them to affect the reduction of the *Juno* Doppler data and require them to be properly modeled. Furthermore, the predicted Doppler signal from tides is a function not only of the Love number and tide-raising body but also of the *Juno*–Io phase angle (bottom panel).

In order to compare the size of the effects of the different Love numbers, Figure 11 shows the signal-to-noise ratio (S/N) during *Juno*'s 13th perijove (PJ13) for Love numbers k_{nm}. The S/N is defined here as the ratio of the nominal value of the Love number and the uncertainty in its estimated value, $\sigma_{k_{nm}}$, from the Doppler data when only the Love number is

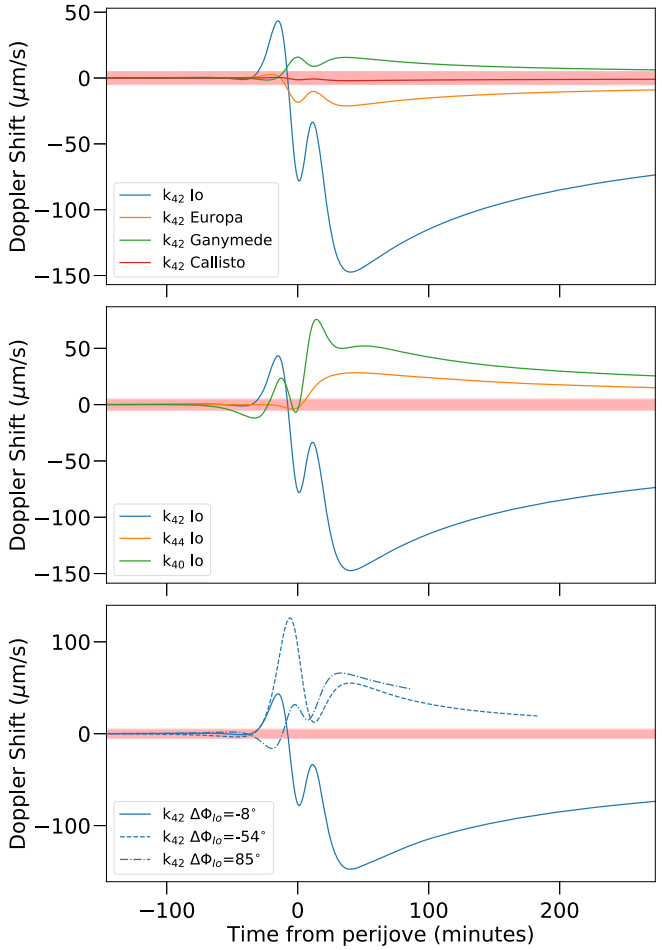

Figure 10. Top panel: Doppler shift as a function of time near *Juno* perijove resulting from adding an equilibrium k_{42} with the magnitude for each Galilean satellite from this paper at their PJ13 positions. The red shaded region shows the noise level for data about the optimized gravity solution for this perijove. Middle panel: same as top panel but showing k_{44}, k_{42}, and k_{40} for Io. Bottom panel: same as top panel but comparing k_{42} from Io for PJ13, PJ06, and PJ03, during which the difference in longitude between *Juno* and Io ($\Delta\Phi_{\rm Io}$) is $-8°$, $-54°$, and $85°$, respectively.

estimated. The uncertainty is given by

$$\sigma_{k_{nm}} = \frac{\sigma_{\dot{\rho}}}{\sqrt{\sum(\partial\dot{\rho}/\partial k_{nm})}}, \tag{20}$$

where the summation is over all Doppler measurements for a single perijove. The S/N is then given by

$$\mathrm{S/N}_{nm} = \frac{k_{nm}}{\sigma_{k_{nm}}}. \tag{21}$$

This definition of the S/N allows a comparison of the amplitude of the effect of the different equilibrium Love numbers on the Doppler measurements. Figure 11 shows that the S/N for Love numbers of degree and order 3 through degree and order 5 ranges from 2 to 2400; hence, most of them are, in principle, detectable in the *Juno* data. In general, the Love numbers cannot be independently estimated because their signatures in the Doppler data are not orthogonal to the other Love numbers, the equilibrium gravity signature, or several other parameters describing other force models. Therefore, *Juno* is likely to be able to accurately estimate values and uncertainties for Love numbers with S/Ns greater than ∼100, but inclusion of

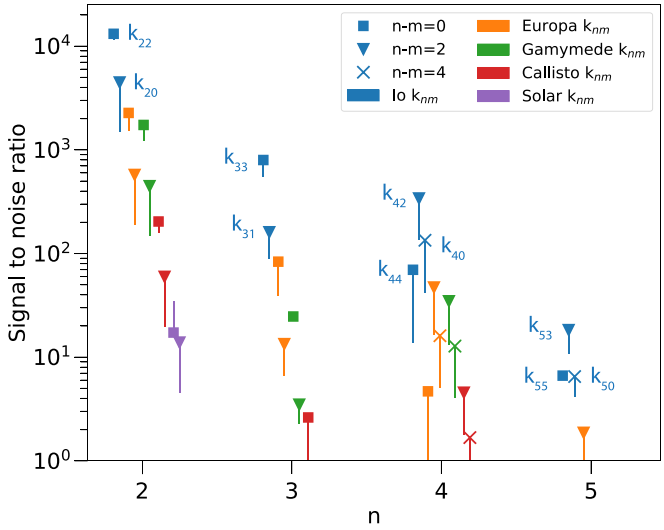

Figure 11. The S/N for time-integrated Doppler shift profiles (Figure 10) resulting from adding the calculated equilibrium k_{nm} for each Galilean satellite and the Sun from this paper at their PJ13 positions. During PJ13, *Juno* was close to the Io subsatellite point ($\Delta\Phi_{\rm Io} = -8°$). The error bars show the range of S/N including two other close approaches, PJ06 and PJ03, with $\Delta\Phi_{\rm Io} = -54°$ and 85°, respectively.

nominal values for lower Love numbers is important to avoid aliasing of small tidal signals into other gravity parameters.

Using this conservative threshold for S/N, Figure 11 suggests that *Juno* will be able to estimate Io's k_{33}, k_{31}, and k_{42}, with k_{44} lying near the threshold. Likewise, it suggests that *Juno* may be able to estimate k_{22} for the other three Galilean satellites. The solar tide is below the threshold, with its k_{22} having an S/N ∼ 30, and the next most significant tidal perturber, Jupiter's satellite Amalthea, yields an S/N an order of magnitude smaller than that of the Sun. If the signals could be sufficiently separated down to an S/N ∼ 10, then degree 3 and 4 Love numbers might be detected for Europa and Ganymede, along with k_{53} for Io. The conclusions of the S/N analysis are, therefore, more optimistic toward the number of detectable k_{nm} values than would be predicted from the gravity anomaly magnitudes alone (Section 3.3). Comparing these predictions to the lower panel of Figure 9 suggests that *Juno* is sensitive to tides with a maximum gravity anomaly as low as ∼1 μgal.

4. Conclusions

In this work, we calculate the equilibrium tidal response of Jupiter to its four Galilean moons and the Sun. We present these as a series of tables that report the k_{nm} for each body, characterizing its dependence on orbital distance, and the estimated uncertainty from the numerical method, physical parameters, interior density structure, and winds. We find an equilibrium $k_{22} = 0.58976 \pm 0.0001$ for Io, consistent with previous calculations (Wahl et al. 2016; Nettelmann 2019), that is remarkably insensitive to the details of the interior structure model, once fitted to the low-degree axisymmetric gravity solution (J_2, J_4, and J_6) from *Juno* (Iess et al. 2018). This means that measurement of k_{22} by *Juno* will not yield additional constraints on the interior structure via the equilibrium tidal response. However, this insensitivity to interior models also means that *Juno* has the opportunity to unambiguously detect dynamic contributions to the tidal response. Should dynamic contributions be detected, they

may yield independent information regarding interior structure or processes, although comprehensive theoretical predictions for such a dynamic response have not been performed.

We introduce improvements to the CMS method for tidal response calculations that eliminate the previously described center-of-mass shift resulting from the original implementation. The improvement allows us to correctly resolve the Love numbers of order $m = 1$ (i.e., k_{31} and k_{51}). We find that for the tides experienced by Jupiter, the predictions of the other k_{nm} values using the previous method (Wahl et al. 2016, 2017a; Nettelmann 2019) are consistent, at least within the expected sensitivity of *Juno*. It remains to be shown whether the improved method has a more profound effect on predictions for close-in extrasolar planets, where the tidal perturbations can be several orders of magnitude stronger.

In Section 3.4 we studied the sensitivity of the *Juno* Doppler measurements to the calculated equilibrium tidal response. By finding the S/N for the calculated k_{nm}, we show that *Juno* is sensitive to both the higher-degree ($n > 2$) Love numbers of Io and the k_{2m} of Europa, Ganymede, Callisto, and the Sun. This is important for two reasons. First, it motivates the need for inclusion of the higher-order tidal components in the analysis and interpretation of *Juno* Doppler data. The signals from these higher-order tides are sufficiently large that mischaracterizing them could lead to their misinterpretation as contributions from another source (i.e., interior density structure or deep winds). Second, they suggest that multiple k_{nm} values may be detectable by *Juno*. In principle, this could provide a test of the theoretical predictions for the rotationally induced splitting and orbital dependence of the equilibrium k_{nm} (Wahl et al. 2017a). They may also offer independent measurements from k_{22} to detect or characterize a dynamic contribution to the tides.

The work of S.W. and B.M. was carried out at the University of California, Berkeley, with the support of the National Aeronautics and Space Administration, *Juno* Program. The work of M.P. and W.M.F. was carried out at the Jet Propulsion Laboratory, California Institute of Technology, under a contract with the National Aeronautics and Space Administration. Government sponsorship is acknowledged.

ORCID iDs

Sean M. Wahl https://orcid.org/0000-0003-2451-7939
Marzia Parisi https://orcid.org/0000-0001-5941-9015
William B. Hubbard https://orcid.org/0000-0003-3185-4538

References

Asmar, S. W., Bolton, S. J., Buccino, D. R., et al. 2017, SSRv, 213, 205
Becker, A., Lorenzen, W., Fortney, J. J., et al. 2015, ApJS, 215, 21
Campbell, J., & Synnott, S. 1985, AJ, 90, 364
Cao, H., & Stevenson, D. J. 2017, JGRE, 122, 686
Chabrier, G., Mazevet, S., & Soubiran, F. 2019, ApJ, 872, 51
Chaplin, W. J., & Miglio, A. 2013, ARA&A, 51, 353
Debras, F., & Chabrier, G. 2019, ApJ, 872, 100
Durante, D., Guillot, T., & Iess, L. 2017, Icar, 282, 174
Folkner, W. M., Iess, L., Anderson, J. D., et al. 2017, GeoRL, 44, 4694
Fuller, J. 2014a, Icar, 242, 283
Fuller, J. W. 2014b, PhD thesis, Cornell Univ.
Gavrilov, S. V., & Zharkov, V. N. 1977, Icar, 32, 443
Guillot, T., Miguel, Y., Militzer, B., et al. 2018, Natur, 555, 227
Hubbard, W. B. 2012, ApJL, 756, L15
Hubbard, W. B. 2013, ApJ, 768, 43
Hubbard, W. B., & Militzer, B. 2016, ApJ, 820, 80
Iess, L., Folkner, W., Durante, D., et al. 2018, Natur, 555, 220
Jacobson, R. A. 2003, JUP230 Orbit Solution, http://ssd.jpl.nasa.gov
Jacobson, R. A. 2013, JUP310 Orbit Solution, http://ssd.jpl.nasa.gov
Kaspi, Y. 2013, GeoRL, 40, 676
Kaspi, Y., Galanti, E., Hubbard, W., et al. 2018, Natur, 555, 223
Kaspi, Y., Guillot, T., Galanti, E., et al. 2017, GeoRL, 44, 5960
Lainey, V., Jacobson, R. A., Tajeddine, R., et al. 2017, Icar, 281, 286
Marley, M. S., & Porco, C. C. 1993, Icar, 106, 508
Miguel, Y., Guillot, T., & Fayon, L. 2016, A&A, 596, A114
Militzer, B. 2009, PhRvB, 79, 155105
Militzer, B. 2013, PhRvB, 87, 014202
Militzer, B., & Hubbard, W. B. 2013, ApJ, 774, 148
Militzer, B., Hubbard, W. B., Vorberger, J., Tamblyn, I., & Bonev, S. A. 2008, ApJL, 688, L45
Militzer, B., Soubiran, F., Wahl, S., & Hubbard, W. 2016, JGRE, 121, 1552
Militzer, B., Wahl, S., & Hubbard, W. B. 2019, ApJ, 879, 78
Morales, M. A., McMahon, J. M., Pierleonie, C., & Ceperley, D. M. 2013, PhRvL, 110, 065702
Murray, C., & Dermott, S. 1999, Solar System Dynamics (Cambridge: Cambridge Univ. Press)
Nettelmann, N. 2017, A&A, 606, A139
Nettelmann, N. 2019, ApJ, 874, 156
Nettelmann, N., Becker, A., Holst, B., & Redmer, R. 2012, ApJ, 750, 52
Nettelmann, N., Holst, B., Kietzmann, A., et al. 2008, ApJ, 683, 1217
Notaro, V., Durante, D., & Iess, L. 2019, P&SS, 175, 34
Perdew, J. P., Burke, K., & Ernzerhof, M. 1996, PhRvL, 77, 3865
Saumon, D., & Guillot, T. 2004, ApJ, 609, 1170
Schöttler, M., & Redmer, R. 2018, JPlPh, 84, 755840401
Seiff, A., Kirk, D. B., Knight, T. C. D., et al. 1998, JGR, 103, 22857
Stevenson, D. J., & Salpeter, E. E. 1977, ApJS, 35, 239
von Zahn, U., Hunten, D. M., & Lehmacher, G. 1998, JGR, 103, 22815
Vorberger, J., Tamblyn, I., Militzer, B., & Bonev, S. 2007, PhRvB, 75, 024206
Wahl, S., Hubbard, W., & Militzer, B. 2016, ApJ, 831, 14
Wahl, S. M., Hubbard, W. B., & Militzer, B. 2017a, Icar, 282, 183
Wahl, S. M., Hubbard, W. B., Militzer, B., et al. 2017b, GeoRL, 44, 4649
Wisdom, J., & Hubbard, W. B. 2016, Icar, 267, 315
Zharkov, V. N., & Trubitsyn, V. P. 1978, Physics of Planetary Interiors (Tucson, AZ: Pachart), 388